Itinerant ferromagnetism of the Pd-terminated polar surface of $PdCoO_2$

Federico Mazzola[a], **Veronika Sunko**[a,b], **Seunghyun Khim**[b], **Helge Rosner**[b], **Pallavi Kushwaha**[b], **Oliver J. Clark**[a], **Lewis Bawden**[a], **Igor Marković**[a,b], **Timur K. Kim**[c], **Moritz Hoesch**[c], **Andrew P. Mackenzie**[b,a,1], **and Phil D. C. King**[a,2]

[a]SUPA, School of Physics and Astronomy, University of St. Andrews, St. Andrews KY16 9SS, United Kingdom; [b]Max Planck Institute for Chemical Physics of Solids, Nöthnitzer Straße 40, 01187 Dresden, Germany; [c]Diamond Light Source, Harwell Campus, Didcot, OX11 0DE, United Kingdom

This manuscript was compiled on October 30, 2018

The ability to modulate the collective properties of correlated electron systems at their interfaces and surfaces underpins the burgeoning field of "designer" quantum materials. Here, we show how an electronic reconstruction driven by surface polarity mediates a Stoner-like magnetic instability to itinerant ferromagnetism at the Pd-terminated surface of the non-magnetic delafossite oxide metal $PdCoO_2$. Combining angle-resolved photoemission spectroscopy and density-functional theory calculations, we show how this leads to a rich multi-band surface electronic structure. We find similar surface state dispersions in $PdCrO_2$, suggesting surface ferromagnetism persists in this sister compound despite its bulk antiferromagnetic order.

Delafossite oxide metals, surface ferromagnetism, electronic reconstruction

Recent advances in the ability to fabricate transition-metal oxides with atomic-scale precision have opened new paradigms for controlling their quantum many-body states and phases (1–10). A prototypical example is the interface between the bulk insulating perovskite oxides $SrTiO_3$ and $LaAlO_3$, which supports a two-dimensional electron liquid (11) hosting a number of remarkable properties, from gate-tuneable superconductivity (12) to magnetic order (13). The emergence of conductivity in this system is thought to be intricately linked to the polar nature of the interface between $SrTiO_3$ and $LaAlO_3$ (11, 14, 15). The carrier densities observed, however, are typically an order of magnitude smaller than would be expected from a pure electronic reconstruction driven by the so-called polar catastrophe (12, 15, 16), and the microscopic mechanism by which polarity may mediate a conducting interface has proved controversial (17–22). It is important, therefore, to investigate the influence of surface and interface polarity in other transition-metal-based oxides, both for developing improved understanding and for expanding the search of materials systems which may host novel surface or interface phases.

Here, we focus on the "ABO_2" delafossite oxides (23–28). Delafossites represent a particularly promising material class both because of their naturally layered structure and the potential to drastically alter their physical properties by changing the A- and B- site cations (29–31). Bulk $MCoO_2$ [M=Pt,Pd] are non-magnetic metals with simple single-band Fermi surfaces. They exhibit the highest conductivity of all known metallic oxides (26, 28, 32–34). They also host polar surfaces, opening the potential to stabilise local electronic environments and phases different to those of the bulk (35–37). We use angle-resolved photoemission spectroscopy (ARPES) to probe the Pd-terminated surface electronic structure of $PdCoO_2$. In agreement with our calculations from density-functional theory (DFT), these experiments demonstrate how the polarity induces a pronounced electron doping at the surface, which in turn mediates an intrinsic Stoner instability towards itinerant ferromagnetism. We find that a similar surface ferromagnetism persists in the sister compound $PdCrO_2$, which is antiferromagnetically ordered in the bulk. This points to an exciting opportunity to utilise polar surfaces and interfaces to induce new magnetic states in oxides as well as to generate naturally-occurring magnetic heterostructures.

Results

Surface termination-dependent measurements. $PdCoO_2$ is comprised of triangular-lattice metallic Pd planes separated by insulating CoO_2 layers. This crystal structure has natural cleavage planes above and below each Pd layer: inequivalent surface terminations would therefore be expected (Fig. 1(a)). Consistent with this, we find a strong variation in the relative intensity of Co $3p$ and Pd $4p$ core levels measured by X-ray photoelectron spectroscopy (XPS) at different patches of the cleaved sample surface (Fig. 1(b)). This is correlated with a marked difference in the electronic structure measured by ARPES (Fig. 1(c-e)). Across the sample, we find a steeply-dispersive state which we attribute as the Pd-derived bulk band (36). In Fig. 1(c), our measurements additionally show

Significance Statement

There has been widespread interest in using interfaces of transition-metal oxides as a platform to control not only their electronic structure, as in semiconductor heterostructures, but also to tune between different collective phases. A major goal is to realise states of the quantum many-body system that are not found in the bulk phase diagrams of the constituent materials. Here, we perform a combined experimental and theoretical study of the delafossite oxide metals $PdCoO_2$ and $PdCrO_2$, finding how electronic reconstructions at their polar surfaces drive instabilities to itinerant surface ferromagnetism. Neither compound supports ferromagnetism in bulk, with $PdCrO_2$ a bulk antiferromagnet, demonstrating how a delicate competition of magnetic correlations can be engineered by intrinsic self-doping at a polar surface or interface.

The ARPES measurements were performed by F.M., V.S., O.J.C., L.B., I.M., and P.D.C.K. and analysed by F.M. H.R. performed the density-functional theory calculations. S.K. and P.K. grew and characterised the samples. T.K.K. and M.H. maintained the experimental ARPES capability and provided experimental support. F.M., V.S., A.P.M. and P.D.C.K. wrote the manuscript with input and discussion from all co-authors, and were responsible for the overall project planning and direction.

To whom correspondence should be addressed. E-mail:[1]andy.mackenzie@cpfs.mpg.de,[2] philip.king@st-andrews.ac.uk

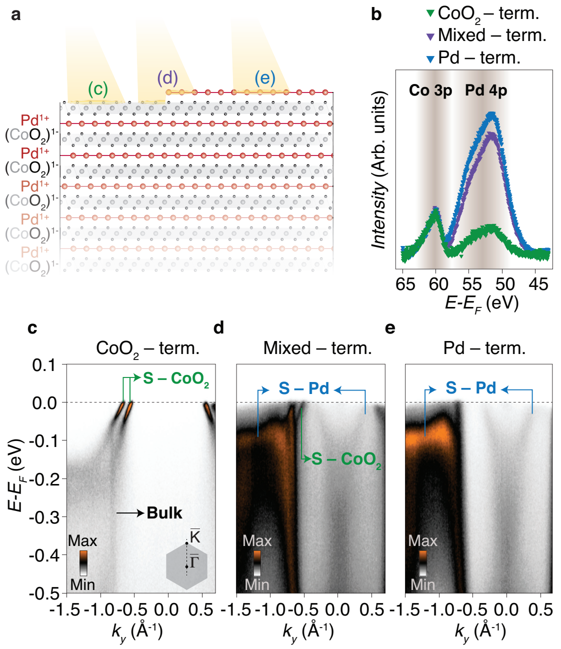

Fig. 1. Surface terminations of $\mathrm{PdCoO_2}$. (a) Side view of the crystal structure of $\mathrm{PdCoO_2}$, showing two possible surface terminations which can be expected. (b) XPS spectra ($h\nu = 120$ eV, after subtraction of a linear background and normalised by the area of the Co 3p peak) at different spatial locations of a cleaved crystal show varying relative ratios of Co and Pd core level peaks, consistent with a spatial dependence of the dominant surface termination. (c-e) Markedly different electronic structures are observed by ARPES ($h\nu = 90$ eV, p-polarisation, measured along $\overline{\Gamma} - \overline{K}$) at these locations, corresponding to predominantly (c) $\mathrm{CoO_2}$, (e) Pd and (d) mixed surface terminations.

a pair of massive hole-like bands (Fig. 1(c), labeled 'S-$\mathrm{CoO_2}$'). These have been assigned previously as surface states from the $\mathrm{CoO_2}$-termination (36, 37), consistent with our XPS measurements from the same sample region, which yield the greatest ratio of Co $3p$: Pd $4p$ core-level spectral weight.

Measurements from a different patch of the same sample (Fig. 1(e)) reveal a completely different surface electronic structure, which we describe in detail below. Our XPS measurements exhibit a much larger spectral weight of the Pd than the Co-derived core-level peak for this sample region (Fig. 1(b)), and we thus attribute these as surface states originating from the Pd-terminated surface ('S-Pd'). We note that for most regions where such states are visible, we observe a superposition of these spectral features with those of the $\mathrm{CoO_2}$-terminated surface (e.g., Fig. 1(d)). This indicates a rather limited spatial extent of typical Pd-terminated regions, with a mixed surface termination within our probing light spot area ($\sim$50 μm diameter). In the following we show our highest-quality ARPES data obtained from a sample which exhibits such a mixed surface terminations. Similar results were obtained from multiple samples.

Pd-terminated surface electronic structure. The measured Fermi surfaces and dispersions from such a mixed surface termination are shown in Fig. 2. The $\mathrm{CoO_2}$-terminated surface states form hexagonal and nearly circular hole-like Fermi surfaces about the Brillouin zone centre, split-off by a surprisingly-large Rashba-like interaction arising due to a large energy scale of inversion symmetry breaking at this surface (37). We do not consider these further here.

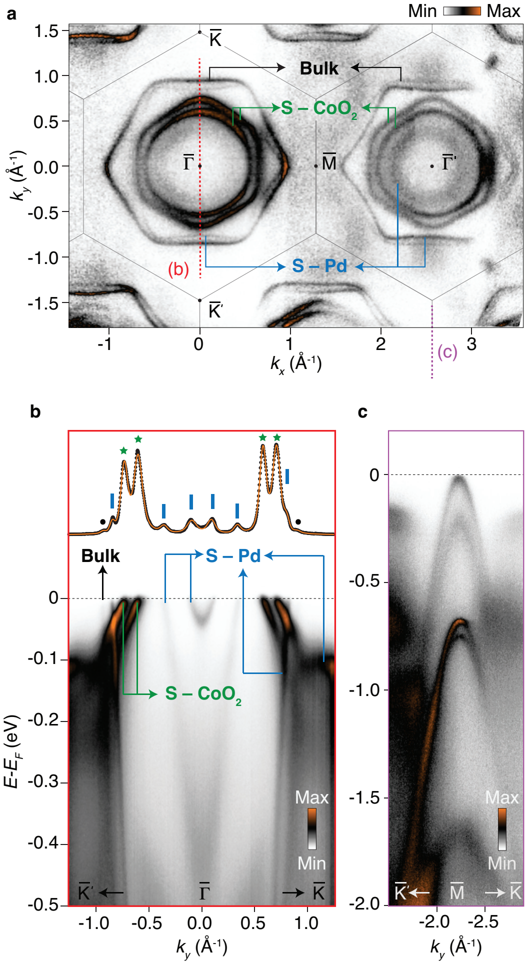

Fig. 2. Surface electronic structure. (a) ARPES Fermi surface ($h\nu = 110$ eV, $E_F \pm 15$ meV, p-pol.) and dispersions ($h\nu = 80$ eV, p-pol.) measured along (b) $\overline{\Gamma} - \overline{K}$ and (c) $\overline{M} - \overline{K}$. As well as the bulk band (Bulk), a series of additional surface states arising from the Pd-terminated (S-Pd) and $\mathrm{CoO_2}$-terminated (S-$\mathrm{CoO_2}$) surfaces are visible. A momentum distribution curve (MDC) at the Fermi level ($E_F \pm 5$ meV) is shown in (b), together with a 12-band peak fit (orange line) and corresponding Fermi momenta (marked by dashes, stars and dots, for S-Pd, S-$\mathrm{CoO_2}$ and bulk, respectively) of such bulk and surface states which cross E_F.

Two larger electron-like Fermi surfaces with sharp linewidths are also visible. From comparison with previous experiments (32, 36), we attribute the largest of these as the Pd-derived bulk Fermi surface. The other has a similar topography, but slightly smaller average k_F, and has greater spectral weight when measured in the second Brillouin zone (Fig. 2(a)). This band is also evident as a steeply-dispersing state in our measured dispersions (Fig. 2(b)), and appears to be an approximate replica of the bulk state, but shifted towards the Fermi level by $\sim$430 meV. In principle, it is not surprising for a polar charge to change the binding energy of states localised at a polar surface. Indeed, for the $\mathrm{CoO_2}$-terminated surface, the absence of Pd atoms above the topmost $\mathrm{CoO_2}$ block leads to a formal valence of 3.5+ rather than 3+ for the surface Co layer, corresponding to an experimentally-observed (35, 37) effective hole-doping of $\approx$0.5 holes/unit cell. Similar electrostatic arguments for the Pd-terminated surface (35) would suggest a formal valence of Pd$^{0.5+}$ at the surface, as compared to

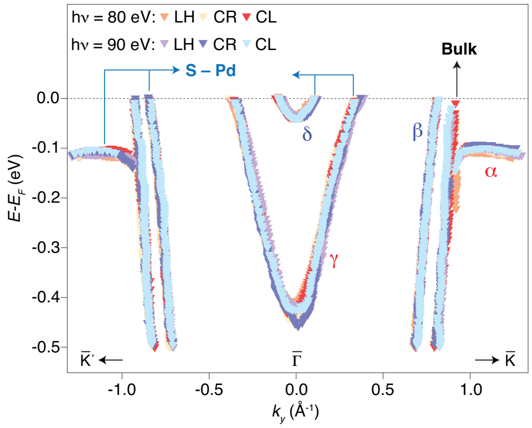

Fig. 3. Itinerant surface ferromagnetism in $PdCoO_2$. Bulk and surface band dispersions exacted from ARPES measurements using different photon energies and light polarisations: linear horizontal (LH, *p*-polarisation), circular right (CR) and circular left (CL) polarisations.

Pd^{1+} in the bulk. This, however, should manifest as a surface doping of $\approx$0.5 electrons/unit cell, seemingly in contrast to the hole-doped copy of the bulk band observed experimentally here.

Moreover, rather than a simple rigid shift of the bulk Pd-derived valence band, our measured dispersions (Fig. 2(b,c)) reveal a much richer surface electronic structure. As well as the steep band discussed above, Fig. 2(b) shows a flat-topped band located $\sim$100 meV below the Fermi level, and a pair of electron-like bands crossing E_F near the Brillouin zone centre (all labeled 'S-Pd' in Fig. 2(b)). The outer of these electron pockets can also be seen in our Fermi surface measurements (Fig. 2(a)), while the innermost band is not clearly observed at the photon energy used. Additionally, multiple fully-occupied bands are found at the Brillouin zone face $\overline{\text{M}}$-point (Fig. 2(c)).

Itinerant surface ferromagnetism. We demonstrate below that such a rich multi-band electronic structure of the Pd-terminated surface of $PdCoO_2$ is the result of an instability to itinerant surface ferromagnetism. Fig. 3 shows the dispersions of the bulk and Pd-derived surface states extracted from the measurements shown in Fig. 2(b) as well as from equivalent measurements performed using a different photon energy and/or light polarisation. These different experimental conditions lead to varying transition matrix elements, selectively enhancing the visibility of different features, (see, for example, SI Appendix, Fig. S1), thus ensuring that we capture the dispersions of all bands accurately. If we assume that these surface states are spin-degenerate and extract their Luttinger count from our experimentally-measured Fermi surfaces, we find an electron count that is unphysically high. In contrast, if we treat them as spin-polarised, we find a surface carrier density that is 0.55 ± 0.03 electrons/unit cell higher than that of the bulk, which is close to the additional 0.5 electrons/unit cell that would be expected from the polar surface charge. We note that spin-polarised states are generically allowed at surfaces, where the breaking of inversion symmetry can lead to a momentum-dependent spin-splitting of the Rashba-type (38). If this was the origin of the surface state spin-polarisation here, however, then the spin-splitting should vanish at the zero-momentum $\overline{\Gamma}$-point, where time-reversal symmetry enforces a Kramers degeneracy. In contrast, the clear splitting of spin-polarised bands that we observe at the $\overline{\Gamma}$ point (Figs. 2(b) and 3) indicates that time-reversal symmetry is broken here (i.e., $E(k=0,\uparrow) \neq E(k=0,\downarrow)$. Moreover, a Rashba-like origin of the observed spin-polarised bands would be incompatible with the large ($\approx$430 meV) energy splitting of the steep bands that we observe, which is more than three times the atomic spin-orbit coupling of Pd.[*] Together, these observations therefore rule out a Rashba origin of our observed spin-polarised surface states; instead, they provide conclusive empirical evidence that the Pd-terminated surface of $PdCoO_2$ is ferromagnetic.

Although the above conclusion is independent of theory, it

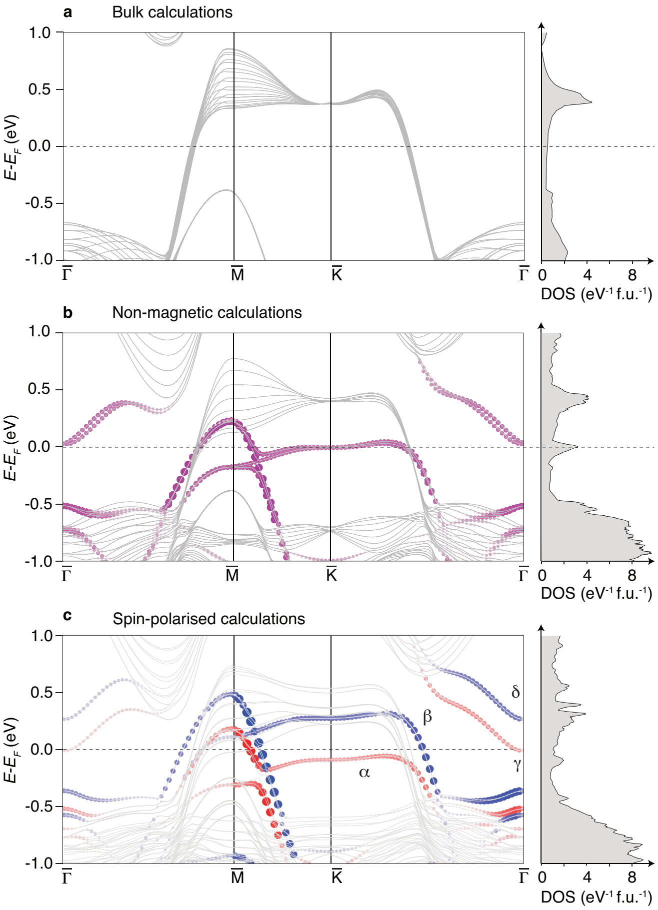

Fig. 4. DFT supercell calculations and electron DOS. (a) Bulk k_z-projected electronic structure of $PdCoO_2$ (left) and corresponding electron DOS (right). (b) Non-magnetic supercell calculations (left), showing the formation of a flat surface state right at the Fermi level, leading to a large peak in the corresponding density of states (right). Additionally, a moderate Rasbha-like spin-orbit splitting of the electron band near the $\overline{\Gamma}$-point is observed. The calculations are projected onto the surface Pd layer (purple colouring) to highlight the surface states. (c) Spin-polarised supercell calculations (left) indicate how a Stoner-like transition spin-splits the states, giving rise to the α-β and γ-δ exchange-split pairs discussed in the main text. The spin majority and minority character as projected onto the surface Pd layer is shown by red and blue colouring, respectively.

---

[*] We note that our non-magnetic calculations (Fig. 4(b), discussed below) show a Rashba-like spin splitting on the order of 50 meV, a realistic value given the atomic spin-orbit strength of ≈ 110 meV. This is, however, significantly smaller than the exchange splitting observed experimentally as well as that found from our spin-polarised calculations. We thus conclude that Rashba-type interactions do not play a significant role here as compared to magnetic correlations. Whether they play a role in determining the detailed magnetic structure, for example in stabilising non-collinear magnetic states, is an interesting question for future study.

is also reinforced by explicit calculations (Fig. 4, see Methods), which further demonstrate how the surface ferromagnetism arises as a result of an intrinsic Stoner-like instability driven by the polar surface charge. This mechanism is shown in Fig. 4. The band which forms the bulk Fermi surface, while steep at the Fermi level (34, 39), becomes much flatter above E_F (evident, for example, along $\bar{\Gamma}$-$\bar{K}$ in the bulk k_z-projected calculations shown in Fig. 4(a)). Compensating the surface polarity should lead to electron doping of the surface layer, as discussed above. This will create a surface copy of the bulk band. Its flat band top, and the high density of states (DOS) associated with it, are pushed downwards towards the Fermi level, as evident in our non-magnetic supercell calculations shown in Fig. 4(b). From a spin-polarised calculation (Fig. 4(c)) we find that the density of states at E_F is sufficiently high to trigger a Stoner transition. The band at the Fermi level therefore exchange splits into a pair of spin-polarised bands (labelled α and β), which can be identified as the experimentally-observed flat (α in Fig. 3) and steep (β) states. Consistent with previous DFT calculations (35), we also find how additional near-E_F surface states inherit a similar exchange splitting, forming the majority-spin and minority-spin γ and δ bands observed at the Brillouin zone centre in our ARPES measurements (Fig. 3).

We note that the surface magnetism observed here is thus qualitatively different to the recent observations of ferromagnetism arising due to uncompensated moments at the surface of, for example, antiferromagnetic (AF) $EuRh_2Si_2$ (40). Instead, it reflects an intrinsic instability of the underlying electronic structure which can be triggered by a pronounced self-doping of the system in response to its polar surface charge. From our extracted Luttinger areas, we estimate a total magnetisation, $M = (N^{\uparrow} - N^{\downarrow})\mu_B = (0.59 \pm 0.03)\mu_B$/unit cell. As the wavefunctions of the surface states are mostly localised on the surface Pd layer (see SI Appendix, Fig. S2), this layer also hosts the largest moment (found to be 0.46 μ_B in our calculations, see Methods). Nonetheless, finite orbital mixing with the subsurface CoO_2 block means that the near-surface Co also inherits a finite, but much smaller, moment, found to be 0.12 μ_B in our calculations.

Ferromagnetic surface of $PdCrO_2$. Finally, we show our measurements of the Pd-terminated surface of the sister compound, $PdCrO_2$ (Fig. 5). As in $PdCoO_2$, the bulk band, which is also responsible for the high bulk conductivity of $PdCrO_2$ (41), is evident as a steeply-dispersing state with the largest k_F. We again observe a copy of this state shifted towards the Fermi level (labeled 'β' in analogy with the $PdCoO_2$ case discussed above), an α-band with its flat top at ≈150 meV below the Fermi level and, in this case, a single electron-like (γ) band crossing E_F near the Brillouin zone centre. This electronic structure is consistent with previous measurements of the chromate (42). Moreover, there is an almost one-to-one correspondence with the surface states that we observe for the Pd-terminated surface of $PdCoO_2$, allowing us to again assign the α and β bands as an exchange-split pair in $PdCrO_2$, and the γ-band as a spin-majority band, with its spin-minority partner being unoccupied. Excitingly, while the CoO_2 layer in $PdCoO_2$ is band insulating and non-magnetic, the CrO_2 layer in bulk $PdCrO_2$ is Mott insulating, and hosts local-moment AF order on the Cr sites (41). Combined with the analysis of $PdCoO_2$ presented above, however, our measurements indicate that $PdCrO_2$ nonetheless also supports ferromagnetism at its Pd-terminated surface.

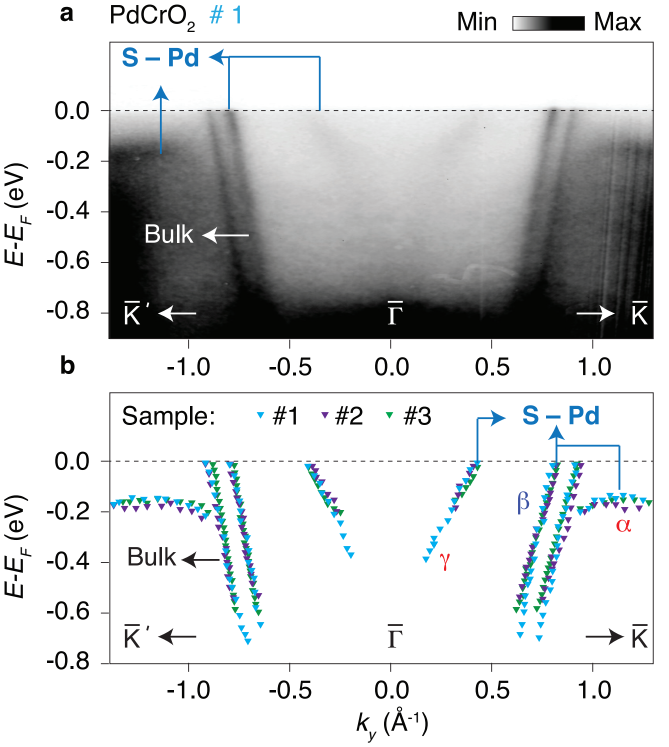

Fig. 5. Itinerant surface ferromagnetism in $PdCrO_2$. (a) ARPES spectra of $PdCrO_2$, measured along the $\bar{\Gamma} - \bar{K}$ direction ($h\nu = 90$ eV, *p*-pol.). (b) Corresponding band dispersions extracted from the data shown in (a) (blue colour), as well as additional band dispersions from other samples (#2, $h\nu = 100$ eV, *p*-pol. and #3, $h\nu = 110$ eV, *p*-pol.). The flat α and steep β exchange-split pair evident in $PdCoO_2$ (Fig. 3(a)) are also observed here, as well as the electron-pocket of the spin-majority γ band. The spin-minority δ band appears to be fully unoccupied.

Discussion

Together, our findings demonstrate how electronic reconstructions at polar surfaces can be exploited to trigger incipient instabilities of the underlying quantum many-body system, here driving a Stoner transition at the Pd-terminated surfaces of $PdCoO_2$ and $PdCrO_2$. This suggests strategies for creating two-dimensional ferromagnets, a topic which has been attracting considerable recent attention in the field of van der Waals materials (43, 44). The co-existence of ferromagnetism with the inherent breaking of inversion symmetry at the surface further opens possibilities to realise significant Dzyaloshinskii-Moriya interactions, providing routes to stabilise modulated magnetic states (45).

Moreover, creating interfaces between disparate magnetic systems offers powerful opportunities for tailoring magnetic interactions (46). This is of both fundamental interest and potential technological applicability, for example enabling the electrical switching of magnetisation in ferromagnetic/antiferromagnetic bilayers (47). Our study indicates how such magnetic heterostructures can naturally be realised at the Pd-terminated surface of $PdCrO_2$. Targeted engineering of magnetic competition could be further aided by the flexibility of the delafossite oxide series. For example, electron doping on the Pd site of $PdCrO_2$ could be used to drive a Stoner transition of the bulk Pd layers, forming an intrinsic superlattice of two-dimensional itinerant ferromagnets and triangular-lattice local-moment antiferromagnets. Polar interfaces of delafossites with other materials provide further routes to create and manipulate rich electronic and magnetic phase diagrams in these systems. More generally, our study further highlights the powerful role that polar interfaces can be expected to play not only in controlling electronic structures, but also for determining the collective phases that can be stabilised, opening routes for the targeted creation and manipulation of multifunctional designer oxide heterostructures.

Note: After preparing our paper for publication, we became aware of an independent study by spin-polarised scanning tunnelling microscopy, which observed real-space signatures of Stoner ferromagnetism at the Pd-terminated surface of $PdCoO_2$, in agreement with the conclusions of our study drawn from a momentum-space perspective (48).

Materials and Methods

Angle-Resolved-Photoemission. Single-crystals of $PdCoO_2$ and $PdCrO_2$ were grown by a flux method in sealed quartz tubes (26, 49). These were cleaved *in situ* at the measurement temperature of $T \sim 10$ K. ARPES measurements were performed at the I05 beamline of Diamond Light Source, UK, using a Scienta R4000 electron analyser and variable light polarisations with photon energies between 60 and 120 eV (50).

Density-functional theory. DFT calculations were performed using the full-potential FPLO code (51–53), utilising the Perdew-Burke-Ernzerhof (54) formalism and including spin-orbit coupling. The surface electronic structure was calculated employing a symmetric slab containing 9 Pd layers, with a vacuum gap of 15 Å. For the inner layers of the slab, the bulk experimental crystal structure (34) was used, while the surface atomic positions were relaxed. We note that, for the unrelaxed surface, we do not stabilse a magnetic state. By fully relaxing the topmost Pd layer to minimise forces on the surface Pd atoms, we obtain a sizable increase of the Pd-O distance, and find a stable ferromagnetic state with a magnetic moment of 0.55 μ_B/unit cell. The moment is predominantly carried by the surface Pd (0.40 μ_B) with minor contributions from the subsurface Co (0.10 μ_B) and O (0.04 μ_B) just below the surface. As shown in SI Appendix Fig. S3, the peak at the Fermi level deriving from the Pd-related surface state becomes considerably narrower for the relaxed surface with the increased Pd-O distance compared to the unrelaxed one. This leads to a strong increase (by about 50%) of the DOS(E_F) and the respective Pd $4d$ DOS, strongly favouring a magnetic splitting of these states in a Stoner picture. The stability of the ferromagnetic surface state slightly increases if not only the surface Pd, but also the CoO_2 layer nearest the surface is relaxed, increasing the magnetic moment to 0.62 μ_B/unit cell (Pd: 0.46 μ_B, Co: 0.12 μ_B, O: 0.05 μ_B). These structural relaxations are used for the calculations presented in the main text. For the DOS shown in Fig. 4, a boxcar smoothing of 25 meV has been used to remove unphysical spikes appearing in the calculated DOS for the supercell.

Experimentally, we find that the surface states at $\overline{\mathrm{M}}$ are all located below E_F (Fig. 2(c)), unlike for our supercell calculations. In general, we note that the exact ordering of bulk and different surface features in our calculations is sensitive to application of a Hubbard U term on the Co sites, as well as an intrinsic off-stoichiometry of the slab due to the polar nature of the structure. Taking into account the strong Coulomb repulsion at the Co-site in a mean field way, applying DFT+U ($U = 4$ eV (37)), the total moment remains almost unchanged, but the contribution of Pd increases sizeably (Pd: 0.54 μ_B, Co: 0.05 μ_B, O: 0.04 μ_B). As a consequence, this leads to a larger splitting in energy of the Pd dominated surface states, as shown in SI Appendix Fig. S4, but does not qualitatively influence any of the conclusions presented here.

ACKNOWLEDGMENTS. We thank C. Hooley for useful discussions. We gratefully acknowledge support from the European Research Council (through the QUESTDO project, 714193), the Engineering and Physical Sciences Research Council, UK (Grant No. EP/I031014/1), the Royal Society, the Max-Planck Society and the International Max-Planck Partnership for Measurement and Observation at the Quantum Limit. VS, LB, and OJC acknowledge EPSRC for PhD studentship support through grant Nos. EP/L015110/1, EP/G03673X/1, and EP/K503162/1, respectively, and IM acknowledges studentship support from the International Max-Planck Research School for Chemistry and Physics of Quantum Materials. We thank Diamond Light Source for access to Beamline I05 (Proposal Nos. SI12469, SI14927, and SI16262) that contributed to the results presented here.

References

1. Mannhart, J. and Schlom, D. J. Oxide interfaces – An opportunity for electronics. *Science* **327,** 1607–1611 (2010).
2. Zubko, P. *et al.,* Interface physics in complex oxide heterostructures. *Annu. Rev. Conden. Ma. P.* **2,** 141–165 (2011).
3. Hwang, H. *et al.,* Emergent phenomena at oxide interfaces. *Nat. Mater.* **11,** 103–113 (2012).
4. Gozar, A. *et al.,* High-temperature interface superconductivity between metallic and insulating copper oxides. *Nature* **455,** 782–785 (2008).
5. Chakhalian, J. *et al.,* Magnetism at the interface between ferromagnetic and superconducting oxides. *Nat. Phys.* **2,** 244–248 (2006).
6. Reyren, N. *et al.,* Superconducting interfaces between insulating oxides. *Science* **317,** 1196–1199 (2007).
7. Boris, A. *et al.,* Dimensionality control of electronic phase transitions in nickel-oxide superlattices. *Science* **332,** 937–940 (2011).
8. Monkman, E. J. *et al.,* Quantum many-body interactions in digital oxide superlattices. *Nat. Mater.* **11,** 855–859 (2012).
9. King, P. D. C. *et al.,* Atomic-scale control of competing electronic phases in ultrathin $LaNiO_3$. *Nat. Nano.* **9,** 443–447 (2014).
10. Wang, Z. *et al.,* Tailoring the nature and strength of electron-phonon interactions in the $SrTiO_3$ (001) 2D electron liquid. *Nat. Mater.* **15,** 835–839 (2016).
11. Ohtomo, A. *et al.,* A high-mobility electron gas at the LaAlO3/SrTiO3 heterointerface. *Nature* **427,** 423–426 (2004).
12. Caviglia, A. D. *et al.,* Electric field control of the LaAlO3/SrTiO3 interface ground state. *Nature* **456,** 624–627 (2008).
13. Brinkman, A. *et al.,* Magnetic effects at the interface between non-magnetic oxides. *Nat. Mater.* **6,** 493–496 (2016).
14. Nakagawa, N. *et al.,* Why some interfaces cannot be sharp. *Nat. Mater.* **5,** 204–209 (2005).
15. Thiel, S. *et al.,* Tunable quasi-two-dimensional electron gases in oxide heterostructures. *Science* **313,** 1942–1945 (2006).
16. Bell, C. *et al.,* Dominant mobility modulation by the electric field effect at the LaAlO3/SrTiO3 interface. *Phys. Rev. Lett.* **103,** 226802 (2009).
17. Siemons, W. *et al.,* Origin of charge density at $LaAlO_3$ on $SrTiO_3$ heterointerfaces: Possibility of intrinsic doping. *Phys. Rev. Lett.* **98,** 216803 (2007).
18. Xie, Y. *et al.,* Control of electronic conduction at an oxide heterointerface using surface polar adsorbates. *Nat. Comm.* **2,** 494 (2011).
19. Yu, L. and Zunger, A. A polarity-induced defect mechanism for conductivity and magnetism at polar–nonpolar oxide interfaces. *Nat. Comm.* **5,** 5118 (2014).
20. Reinle-Schmitt, M. L. *et al.,* Tunable conductivity threshold at polar oxide interfaces. *Nat. Comm.* **12,** 2846 – 2851 (2012).
21. Bristowe, N. C. *et al.,* Surface defects and conduction in polar oxide heterostructures. *Phys. Rev. B* **83,** 205405 (2011).
22. Gariglio, S. *et al.,* Research update: conductivity and beyond at the $LaAlO_3$/$SrTiO_3$ interface. *APL Mat.* **4,** 060701 (2016).
23. Shannon, R. D. *et al.,* Chemistry of noble metal oxides. II. Crystal structures of platinum cobalt dioxide, palladium cobalt dioxide, coppper iron dioxide, and silver iron dioxide. *Inorganic Chem.* **10,** 719–723 (1971).
24. Shannon, R. D. *et al.,* Chemistry of noble metal oxides. I. Syntheses and properties of ABO_2 delafossite compounds. *Inorganic Chem.* **10,** 713–718 (1971).
25. Shannon, R. D. *et al.,* Chemistry of noble metal oxides. III. Electrical transport properties and crystal chemistry of ABO_2 compounds with the delafossite structure. *Inorganic Chem.* **10,** 723–727 (1971).
26. Tanaka, M. *et al.,* Growth and Anisotropic Physical Properties of $PdCoO_2$ Single Crystals. *J. Phys. Soc. J.* **65,** 3973–3977 (1996).
27. Takatsu, H. *et al.,* Roles of High-Frequency Optical Phonons in the Physical Properties of the Conductive Delafossite $PdCoO_2$. *J. Phys. Soc. J.* **76,** 104701 (2007).
28. Mackenzie, A. P., The properties of ultrapure delafossite metals. *Rep. Prog. Phys.* **80,** 032501 (2017).
29. Cheong, S. W. and Mostovoy, M. Multiferroics: a magnetic twist for ferroelectricity. *Nat. Mater.* **6,** 1476-1122 (2007).
30. Kawazoe, H. *et al.,* P-type electrical conduction in transparent thin films of $CuAlO_2$. *Nature* **389,** 939–942 (1997).
31. Singh, D. J. Electronic and thermoelectric properties of $CuCoO_2$ Density functional calculations. *Phys. Rev. B* **76,** 085110 (2007).
32. Hicks, C. W. *et al.,* Quantum Oscillations and High Carrier Mobility in the Delafossite $PdCoO_2$. *Phys. Rev. Lett.* **109,** 116401 (2012).
33. Takatsu, H. *et al.,* Extremely Large Magnetoresistance in the Nonmagnetic Metal $PdCoO_2$. *Phys. Rev. Lett.* **111,** 056601 (2013).

34. Kushwaha, P. *et al.,* Nearly free electrons in a 5d delafossite oxide metal. *Science Adv.* **1,** e1500692 (2015).
35. Kim, K. *et al.,* Fermi surface and surface electronic structure of delafossite $\mathrm{PdCoO_2}$. *Phys. Rev. B* **80,** 035116 (2009).
36. Noh, H. J. *et al.,* Anisotropic electric conductivity of delafossite $\mathrm{PdCoO_2}$ studied by Angle-Resolved Photoemission Spectroscopy. *Phys. Rev. Lett.* **102,** 256404 (2009).
37. Sunko, V. *et al.,* Maximal Rashba-like spin splitting via kinetic-energy-coupled inversion-symmetry breaking. *Nature* **549,** 492–496 (2017).
38. Bychkov, Y. A. and Rashba, E. I. Properties of a 2D electron gas with lifted spectral degeneracy. *JETP Lett.* **39,** 78-81 (1984).
39. Noh, H. J. *et al.,* Orbital character of the conduction band of delafossite $\mathrm{PdCoO_2}$ studied by polarization-dependent soft x-ray absorption spectroscopy. *Phys. Rev. B* **80,** 073104 (2009).
40. Chikina, A. *et al.,* Strong ferromagnetism at the surface of an antiferromagnet caused by buried magnetic moments. *Nat. Commun.* **5,** 3171 EP (2014).
41. Takatsu, H. *et al.,* Critical behavior of the metallic triangular-lattice Heisenberg antiferromagnet $\mathrm{PdCrO_2}$. *Ann. Rev. of Mat. Res.* **79,** 104424 (2009).
42. Sobota, J. A. *et al.,* Electronic structure of the metallic antiferromagnet $\mathrm{PdCrO_2}$ measured by angle-resolved photoemission spectroscopy. *Phys. Rev. B* **88,** 125109 (2013).
43. Huang, B. *et al.,* Layer-dependent ferromagnetism in a van der Waals crystal down to the monolayer limit. *Nature* **546,** 270-273 (2017).
44. Gong, C. *et al.,* Discovery of intrinsic ferromagnetism in 2D van der Waals crystals. *Nature* **546,** 265-269 (2017).
45. Banerjee, S. *et al.,* Ferromagnetic exchange, spin–orbit coupling and spiral magnetism at the $\mathrm{LaAlO_3/SrTiO_3}$ interface. *Nat. Phys.* **9,** 626–630 (2013).
46. Bhattacharya, A. and May, S. J. Magnetic Oxide Heterostructures. *Phys. Rev. B* **44,** 65-90 (2014).
47. Fukami, S. *et al.,* Magnetization switching by spin-orbit torque in an antiferromagnet–ferromagnet bilayer system. *Nat. Mat.* **15,** 535–541 (2016).
48. Jung, J., Lee, J., *et al., to be published* (2018).
49. Takatsu, H. *et al.,* Single crystal growth of the metallic triangular-lattice antiferromagnet $\mathrm{PdCrO_2}$. *Journal of Crystal Growth* **312,** 3461 (2010).
50. Hoesch, M. *et al.,* A facility for the analysis of the electronic structures of solids and their surfaces by synchrotron radiation photoelectron spectroscopy. *Rev. of Scientific Inst.* **88,** 013106 (2017).
51. Koepernik, K. *et al.,* Full-potential nonorthogonal local-orbital minimum-basis band-structure scheme. *Phys. Rev. B* **59,** 1743–1757 (1999).
52. Opahle, I. *et al.,* Full-potential band-structure calculation of iron pyrite. *Phys. Rev. B* **60,** 14035–14041 (1999).
53. http://www.fplo.de, version fplo14.00-47
54. Perdew, J. P. *et al.,* Generalized Gradient Approximation made simple. *Phys. Rev. Lett.* **77,** 3865–3868 (1996).